Physical and numerical investigation of the flow induced vibration of the hydrofoil

Q Wu, G Y Wang, B Huang

Beijing Institute of Technology, 5 South Zhongguancun Street, Beijing 100081, China

E-mail: wangguoyu@bit.edu.cn

Abstract. The objective of this paper is to investigate the flow induced vibration of a flexible hydrofoil in cavitating flows via combined experimental and numerical studies. The experiments are presented for the modified NACA66 hydrofoil made of POM Polyacetate in the closed-loop cavitation tunnel at Beijing Institute of Technology. The high-speed camera and the single point Laser Doppler Vibrometer are applied to analyze the transient flow structures and the corresponding structural vibration characteristics. The hybrid coupled fluid structure interaction model is conducted to couple the incompressible and unsteady Reynolds Averaged Navier-Stokes solver with a simplified two-degree-of-freedom structural model. The *k-ω* SST turbulence model with the turbulence viscosity correction and the Zwart cavitation model are introduced to the present simulations. The results showed that with the decreasing of the cavitation number, the cavitating flows display incipient cavitation, sheet cavitation, cloud cavitation and supercavitation. The vibration magnitude increases dramatically for the cloud cavitation and decline for the supercavitation. The cloud cavitation development strongly affects the vibration response, which is corresponding to the periodically developing and shedding of the large-scale cloud cavity. The main frequency of the vibration amplitude is accordance with the cavity shedding frequency and other two frequencies of the vibration amplitude are corresponding to the natural frequencies of the bending and twisting modes.

1. Introduction

Cavitation generally occurs when the local fluid pressure reduces to the saturated vapor pressure and consequently bubbles filled with vapor. Since it can lead to many problems such as pressure pulsations, vibration, noise and erosion [1-3], it is necessary to understand the influence of unsteady cavitation on the flow induced vibrations, which in turn affects the unsteady cavitating flow behaviors. Amromin and Kovinskaya [4] analyzed the vibration of an elastic hydrofoil with an attached cavity in periodically perturbed flow and the results showed that the structural vibration increased significantly due to the cavitation. Torre et al. [5] experimentally investigated the influence of the sheet cavitation and supercavitation on the added mass effects experienced by a modified NACA0009 hydrofoil. The results showed that the added mass decreases when cavitation appears because of the increased cavity length. Almost these related studies have been done by utilizing the experimental technique, and recent advancement of the numerical technique has made it possible to simulate the turbulent flows around flexible hydrofoils. Ausoni et al. [6] conducted the experimental and numerical studies to investigate the effects of cavitation and fluid-structure interaction on vortex generation mechanism. They found that the vortex-induced vibration level significantly increased at cavitation onset and the transverse velocity at the hydrofoil trailing edge increased the vortex strength. Young et al. [7]

developed a new hybrid coupling algorithm and evaluated the predictive capability of the above fluid structure interaction approaches for the simulations of the forced pitching response of a steel and a plastic hydrofoil. They reported that the new hybrid coupling algorithm can converge faster and avoid the numerical instability issues associated with artificial added-mass effects effectively.

Although the phenomenon of cavitation and flow induced vibration has been studied, a brief review of these recent works indicates that we still have inadequate understanding on the correlation between the structural vibration velocity and the transient cavitating flow patterns. The objective of this work is to shed light on the unsteady cavitating flow and corresponding vibration characteristics, and to offer a basis for future numerical validation studies.

2. Experimental setup

Experimental studies are conducted in a closed-loop cavitation tunnel at Beijing Institute of Technology [8], as shown in Fig. 1, with the test section being 0.7m (length)×0.07m (width)×0.19m (height). The upstream pressure and the flow velocity are measured by the vacuometer (with the uncertainty 0.25% of the maximum range) and the electromagnetic flowmeter (with the uncertainty 0.5% of the maximum range) respectively. The modified-NACA66, made of POM Polyacetate, is adopted in the present study. And it has a uniform cross-section of shape with chord length c=0.075m, the span b=0.069m and a maximum thickness-to-chord ratio of 12%.

Figure 2 shows the layout of the experimental system. The hydrofoil is made of POM Polyacetate with Young's modulus of E_s=3GPa,ρ_s=1480kg/m^3, and v_s=0.35. The cavitation patterns are documented by a high-speed camera (HG-LE, by Redlake) with a sampling frequency of 2500 fps, and the vibration velocities are measured with a single point Laser Doppler Vibrometer (Polytec PSV-100). with a sample frequency of 22kHz. The digital low pass filter with the cutoff frequency of 5kHz has been applied to recover an accurate description of the main frequencies and suppress noise at higher frequencies. Then the signal can be fed into digital inputs of a data acquisition system (NI X Series Multifunction Data Acquisition) with the sampling rate of 20.48kHz, followed by a three-level 1-D wavelet analysis using the Haar wavelet [9] to de-noise the signal.

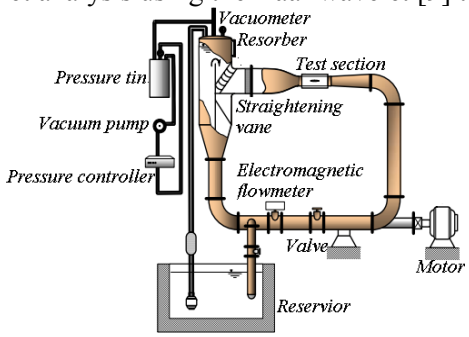

Figure 1 Schematic of the cavitation tunnel

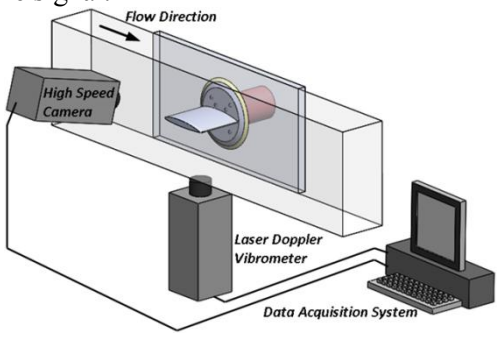

Figure 2 Layout of the experimental system

3. Numerical model

3.1. Fluid model

The current simulation solves the incompressible and unsteady Reynolds Average Navier-Stokes (URANS) equations using the k-ω SST turbulence model [10], which applies the k-ε model away from the wall and the k-ω model near the wall. In order to consider the local compressibility effect of multiphase mixtures on the turbulence model, the turbulent viscosity is revised [11].

$$\frac{\partial(\rho_m k)}{\partial t}+\frac{\partial(\rho_m U_j k)}{\partial x_j}=P_k-D_k+\frac{\partial}{\partial x_i}\left[(\mu_m+\frac{\mu_t}{\sigma_k})\frac{\partial k}{\partial x_i}\right] \quad (1)$$

$$\frac{\partial(\rho_m \omega)}{\partial t}+\frac{\partial(\rho_m U_j \omega)}{\partial x_j}=C_\omega P_\omega-\beta_\omega\rho_m\omega^2+\frac{\partial}{\partial x_i}\left[(\mu_m+\frac{\mu_t}{\sigma_k})\frac{\partial \omega}{\partial x_i}\right]+2\rho_m(1-F_1)\sigma_{\omega 2}\frac{1}{\omega}\frac{\partial k}{\partial x_i}\frac{\partial \omega}{\partial x_i} \quad (2)$$

The viscosity is defined as:

$$\mu_t = \frac{\rho a_1 k}{\max(a_1\omega;\ SF_2)},\ \mu_{t\_\mathrm{mod}} = \mu_t f(n),\quad f(n) = \frac{\rho_v + (1-\alpha_v)^n(\rho_l - \rho_v)}{\rho_v + (1-\alpha_v)(\rho_l - \rho_v)} \tag{3}$$

where ρ_m is the mixture fluid density, ρ_l and ρ_v are the liquid and vapor densities respectively, U is the velocity, P is the pressure, μ_m is the mixture laminar viscosity, μ_t is the turbulent viscosity. The subscripts i, j denote the directions of the Cartesian coordinates. n=3 is chosen and the validation studies can be referred to Huang et al. [12].

In this work, the Zwart cavitation model [13] is used, which assumes a constant nuclei size and density in the fluid domain. The source term $\dot{m}^+$ and sink term $\dot{m}^-$ can be defined as follows:

$$\frac{\partial(\rho_l\alpha_l)}{\partial t} + \frac{\partial(\rho_l\alpha_l u_j)}{\partial x_j} = \dot{m}^+ + \dot{m}^- \tag{4}$$

$$\dot{m}^- = -C_{dest}\frac{3\alpha_{nuc}(1-\alpha_v)\rho_v}{R_B}\left(\frac{2}{3}\frac{p_v - p}{\rho_l}\right)^{1/2},\ p < p_v;\quad \dot{m}^+ = C_{prod}\frac{3\alpha_v\rho_v}{R_B}\left(\frac{2}{3}\frac{p - p_v}{\rho_l}\right)^{1/2},\ p > p_v \tag{5}$$

where C_{dest} is the constant generation rate of vapor in the region where the local pressure is less than the vapor pressure and C_{prod} is the constant rate for re-conversion of vapor back to liquid in a region where the local pressure exceeds the vapor pressure. In the present study, the model constants are assumed as the default values in CFX [14].

3.2. Solid model

The cantilevered hydrofoil with the bending and twisting flexibility is modeled as a chord-wise rigid, two degree of freedom system in this work. Both the bending deformation h and twisting deformation θ are defined about the elastic axis, which is located at the mid-chord of the foil. The governing equation of the 2-DOF system motion without external excitation forces can be written as:

$$\begin{bmatrix} m & S_\theta \\ S_\theta & I_\theta \end{bmatrix}\begin{Bmatrix} \ddot{h} \\ \ddot{\theta} \end{Bmatrix} + \begin{bmatrix} C_h & 0 \\ 0 & C_\theta \end{bmatrix}\begin{Bmatrix} \dot{h} \\ \dot{\theta} \end{Bmatrix} + \begin{bmatrix} K_h & 0 \\ 0 & K_\theta \end{bmatrix}\begin{Bmatrix} h \\ \theta \end{Bmatrix} = \begin{Bmatrix} L \\ M \end{Bmatrix} \tag{6}$$

where m, S_θ, I_θ are the structural mass, the static imbalance and the moment of inertia respectively, C_h and C_θ are the structural damping values for the bending and twisting motions respectively, K_h and K_θ are the structural bending and torsional stiffness values respectively. h, $\dot{h}$ and $\ddot{h}$ are the bending displacement, velocity, and acceleration, while θ, $\dot{\theta}$, $\ddot{\theta}$ are the twisting displacement, velocity, and acceleration. L and M are the fluid lift (be positive along the Y-axis) and moment (be positive as the counter-clockwise direction) acting on the hydrofoil, which are computed by the fluid solver.

3.3. Fluid structure interaction model

According to the hybrid coupled fluid structure interaction model, the equation of motion, Equation (6), is discretized in the time-domain:

$$\begin{bmatrix} m & S_\theta \\ S_\theta & I_\theta \end{bmatrix}\begin{Bmatrix} \ddot{h} \\ \ddot{\theta} \end{Bmatrix}_{n+1}^{i+1} + \begin{bmatrix} C_h & 0 \\ 0 & C_\theta \end{bmatrix}\begin{Bmatrix} \dot{h} \\ \dot{\theta} \end{Bmatrix}_{n+1}^{i+1} + \begin{bmatrix} K_h & 0 \\ 0 & K_\theta \end{bmatrix}\begin{Bmatrix} h \\ \theta \end{Bmatrix}_{n+1}^{i+1} - \begin{Bmatrix} L_{fluid}^T \\ M_{fluid}^T \end{Bmatrix}_{n+1}^{i+1} = \begin{Bmatrix} L \\ M \end{Bmatrix}_{n+1}^{i} - \begin{Bmatrix} L_{fluid}^T \\ M_{fluid}^T \end{Bmatrix}_{n+1}^{i} \tag{7}$$

where i is the sub-iteration number within each time step n, L_{fluid}^T and M_{fluid}^T subtracted from the left and right sides of the equation are the potential flow estimate of the hydroelastic force and momentum, which is proposed by Theodorsen [15] to account for the effects of fluid inertial, damping and restoring forces in each time step and sub-iteration, avoiding the over-estimation of the structural displacement. The detailed mass, damping and stiffness matrixes can be referred to [8].

3.4. Numerical setup

The simulation is conducted with a 2D fluid solver and the computational domain is given according to the experimental setup, as shown in Fig. 3. The hydrofoil fixes at α_0=8°, with the inlet velocity set as U_∞=8m/s, which is calculated based on the flow rate measured by the electromagnetic flowmeter

and the section area of the test section. According to [16], a constant turbulent intensity of 1% set at the inlet boundary. The outlet pressure is set according to the cavitation number $\sigma=(p_\infty-p_v)/(0.5\rho_l U_\infty^2)$, which is consistent with the absolute pressure measured in the experiment via the vacuum pump. A no-slip boundary condition is imposed on the hydrofoil surface and symmetry conditions are imposed on the side walls of the fluid domain. The numerical mesh is shown in Fig. 4, composed of 110,000 structured elements and 226,000 nodes. The mesh is refined near the leading and trailing edge of the foil and in the wake region to satisfy $y^+=yu_\tau/\nu\approx1$, where y is the thickness of the first cell from the foil surface, and u_τ is the wall frictional velocity.

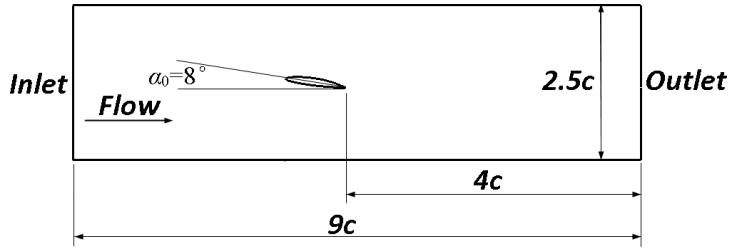

Figure 3 Computational domain

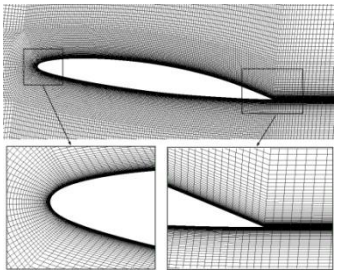

Figure 4 Fluid mesh details

4. Results and discussions

4.1. The typical cavity shapes and flow induced vibration amplitudes in different cavitation regimes

Figure 5 shows the typical cavity shapes observed in the experimental visualization and predicted in the numerical simulation for different cavitation regimes with σ=2.0, 1.2, 0.8 and 0.5. With the decreasing of the cavitation number, the cavitating flows display incipient cavitation containing some micro-sized vapor bubbles at leading edge of the foil, sheet cavitation with unsteady small bubbly vortices at the rear portion of the cavity, cloud cavitation with a quasi-periodic pattern and supercavitation with the relative stable cavity covering the entire hydrofoil. The time-averaged cavity lengths L/c and the maximum normalized vibration amplitude $\delta y/c$ against $\sigma/2\alpha$ for various cavitation regimes are shown in Fig. 6. The results showed that the mean cavity lengths decrease with the increase of $\sigma/2\alpha$, while as for the maximum vibration amplitude, it keeps relative small for the incipient and sheet cavitation, and increases dramatically for the cloud cavitation when the sheet cavity grows and the trailing edge becomes increasingly unsteady accompanied with cloud cavities shedding massively. After that, a sharp decline of the vibration amplitude can be observed for the supercavitation. This is mainly because when the supercavitation occurs, the cavitating area covers the entire hydrofoil and the flow field has a relative steady characteristics.

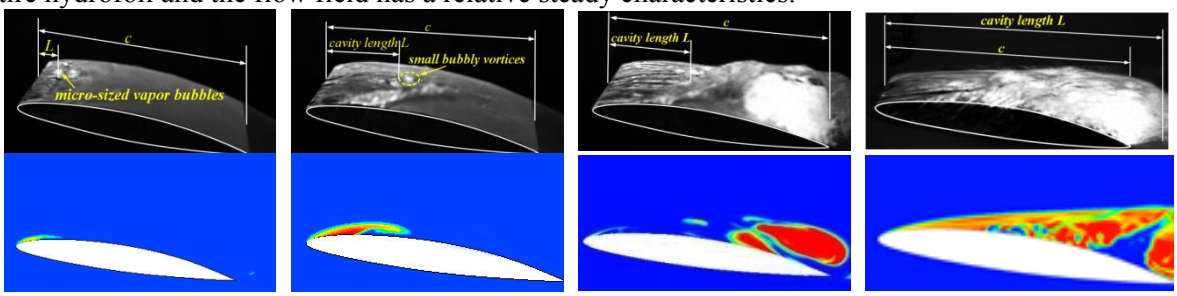

(a) σ=2.0 incipient cavitation (b) σ=1.2 sheet cavitation (c) σ=0.8 cloud cavitation (d) σ=0.5 supercavitation

Figure 5 The typical cavitation patterns for different cavitation regimes

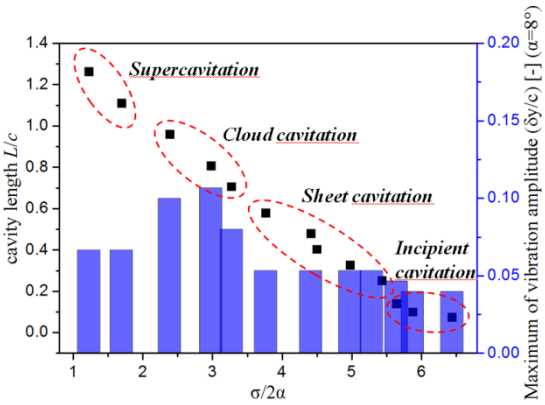

Figure 6 The measured normalized cavity length (L/c) (the separate points) and the maximum of the vibration amplitude (δy/c) against σ/2α (the blue columns) for different cavitation regimes

4.2. The cloud cavitation behaviors and the corresponding flow induced vibration chatacteristics

4.2.1. The cavitating flow patterns. As to the regime of the cloud cavitation, the unsteady breakdown and shedding of the cavity occurs violently, which may lead to strong dynamic instabilities. Figure 7 shows the evolution of cavitating flow patterns observed from the front and top view during the experiment, along with the numerically predicted vapor fractions and vorticity contours (the vorticity with negative value is defined as clockwise vortex and the positive value is defined as counter-clockwise vortex) at representative times. Overall, reasonable agreement is obtained between the predicted and observed cavity patterns. At initial time of a period (t_1), as shown in Figure 7(a), the partial sheet cavity begins to form at the leading edge of the foil. From t_2 to t_3, as shown in Figs. 7(b)-(c), the cavity develops on the suction side of the foil and the re-entrant jet begins to form at the rear end of the cavity due to the high reverse pressure gradient. Between t_4 and t_5, the existing cavity is lifted away from the wall as the re-entrant jet reaches the vicinity of the leading edge and meanwhile, the cloud cavity with high vapor fraction sheds downstream. Due to the great flexibility of the hydrofoil, which is also closely related to the instability of the cavitating flow structures, the cavity partially collapses with the vibration and breaks into several medium-scale cloud cavities, as shown in Fig. 7(e). Governed by the main flow, the shedding cavitating vortex structures are transported towards the trailing edge of the foil and interacts with the downstream counter-clockwise trailing edge vortex, resulting that two counter-rotating vortices with cavitating cores shed, as shown in Figures 7(b)-(c), followed by the formation of the partial sheet cavity in the next period.

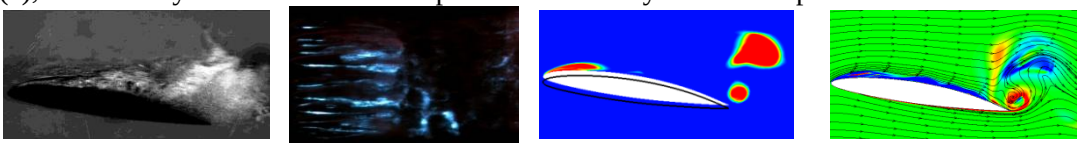

(a) $t_1=t_0$

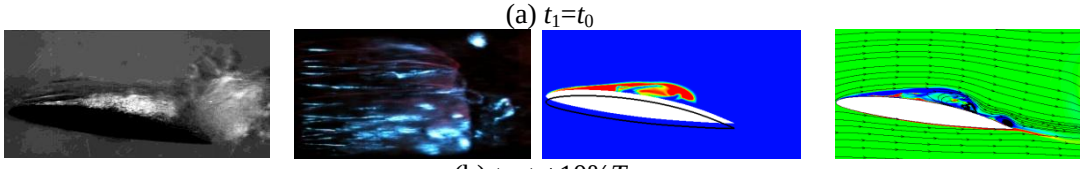

(b) $t_2=t_0+10\%T_{ref}$

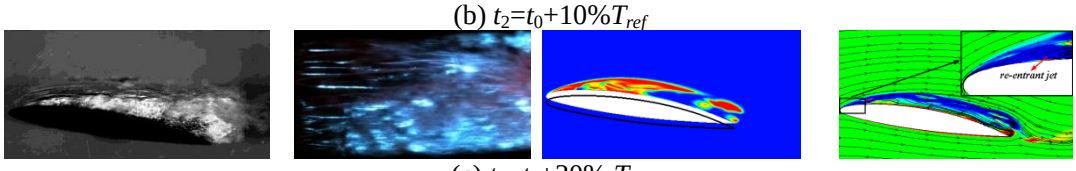

(c) $t_3=t_0+30\%\ T_{ref}$

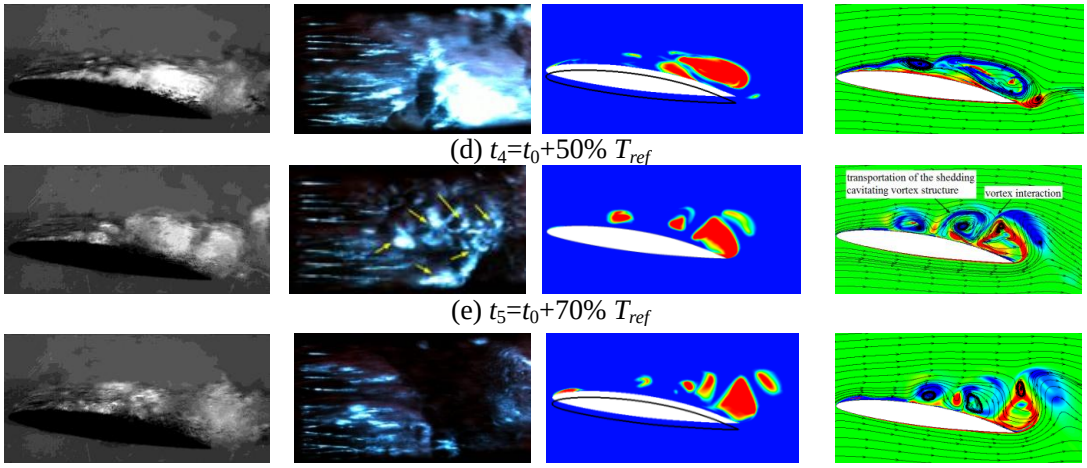

(d) $t_4=t_0+50\%\ T_{ref}$

(e) $t_5=t_0+70\%\ T_{ref}$

(f) $t_6=t_0+80\%\ T_{ref}$

Figure 7 Experimental observation of the cavitation patterns and predicted vapor fraction contours.

4.2.2. The flow induced vibration characteristics. In order to investigate the vibration characteristics of the hydrofoil, Figure 8 shows the measured and predicted natural frequencies of the hydrofoil, and the corresponding schematic view of these mode shapes obtained from the numerical simulation is also presented. The experiment was performed with the test section which is full of water and made by analyzing the vibration response to individual shock. The response of the structure is formulated with a 3D finite element domain using the commercial finite element solver ANSYS Workbench. The fluid domain is modeled using a higher order 3-D 20-node element Fluid220 and Fluid221, and the structure domain is modeled using a higher order 3-D 20-node solid element Solid186 and Solid187. Hence the mass and stiffness matrix can be calculated based on the material properties and the geometry. Reasonable agreement can be obtained between the experimental and numerical results. The first mode is a bending mode with the measured and calculated value of 102Hz and 98Hz respectively. The second mode, which corresponds to the torsion mode, is 167Hz and 171Hz according to the experimental and numerical results. The measured and predicted third mode is 213Hz and 215Hz respectively.

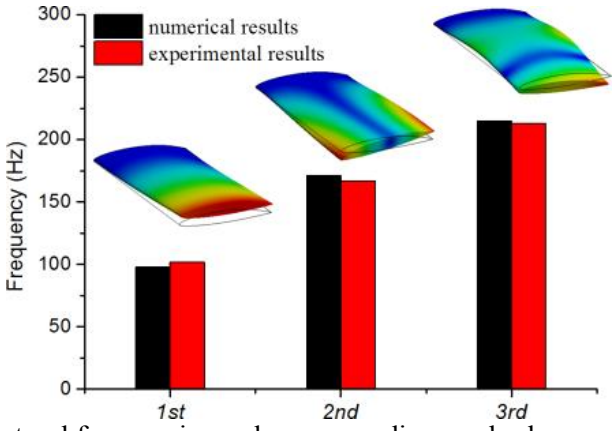

Figure 8 The natural frequencies and corresponding mode shapes of the hydrofoil

To further investigate the effect of cavitation behavior on the flow-induced vibration, the vibration amplitude and the corresponding frequency spectrum have been analysed. Figure 9 shows the measured time evolution of the vibration amplitude of the hydrofoil, which is computed from the integral of the LDV velocity signal, along with the structural displacement predicted in the numerical simulation. It is observed that the cavitation development strongly affects the vibration response, which is corresponding to the periodically developing and shedding of the large-scale cloud cavity. Figure 10 shows the frequency spectrum of the measured vibration amplitude. From the spectra of the

vibration amplitude, the primary flow induced frequency is about 16Hz, which is corresponding to the cavity shedding frequency. While other two amplitude peaks can be observed at about 100Hz and 168Hz, which are attributed to the natural frequencies of the bending and twisting modes. It should be noted that the vortex shedding frequency in present study is about 145Hz, with the ratio of vortex shedding frequency to the structure natural frequencies is 1.45 and 0.86.

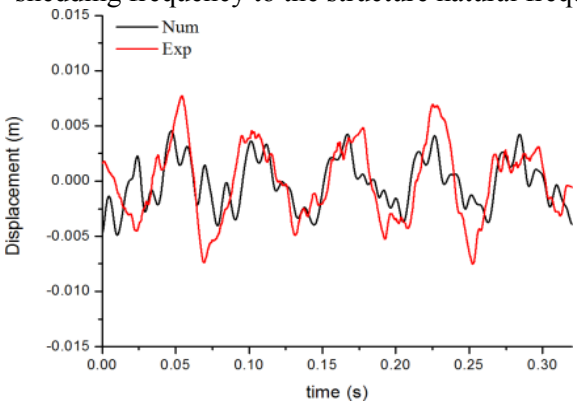

Figure 9 Evolution of the vibration amplitude

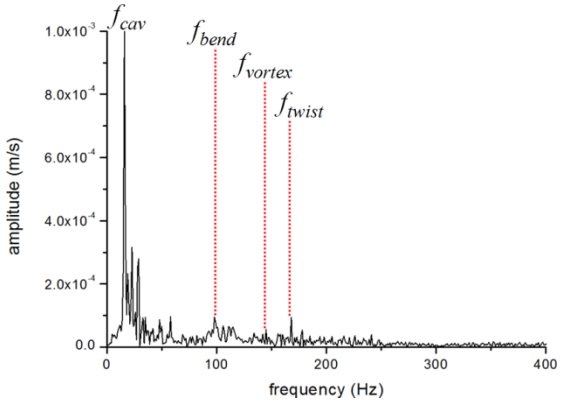

Figure 10 Frequency spectrum of vibration amplitude

5. Conclusions

In this paper, the unsteady cavitating flow around a modified NACA66 hydrofoil and corresponding flow-induced vibration characteristics are studied. The primary findings include:

1) With the decreasing of the cavitation number, the cavitating flows display incipient cavitation, sheet cavitation, cloud cavitation and supercavitation. The corresponding vibration magnitude changes with different cavitation regimes: maximum vibration amplitude keeps relative small for the inception cavition and sheet cavitation, and increases dramatically for the cloud cavitation because of the increasing unsteadiness of cavity structures around the hydrofoil. The mean cavity lengths decrease with the increase of the cavitation number. The increase of the maximum vibration amplitude for the cloud cavitation is due to the unsteady cavity shedding and a sharp decline of the vibration amplitude for the supercavitation is mainly because of the relative steady characteristics in that stage.

2) For the cloud cavitation regime, the partial sheet cavity is formed at initial time of a period and develops along with the formation of the re-entrant jet. As the re-entrant jet reaches the vicinity of the leading edge, the cloud cavity with high vapor fraction sheds downstream, with the interaction between counter-rotating vortices, which result to the final shedding of the whole cavities as well as the vortex structures.

3) The cavitation development strongly affects the vibration response, which is corresponding to the periodically developing and shedding of the large-scale cloud cavity, with the main frequency is accordance with the cavity shedding frequency and other two vibration frequencies are corresponding to the bending and twisting frequency.

Acknowledgments

The authors gratefully acknowledge the support by the National Natural Science Foundation of China (Grant Nos.: 51306020 and 11172040), the Natural Science Foundation of Beijing (Grant No. 3144034), the Excellent Young Scholars Research Fund of Beijing Institute of Technology and the China Scholarship Council (No.201506030091).

References

[1] Joseph D D 1995 Cavitation in a flowing liquid *Phys. Rev. E* **51** 1649-1650

[2] Paik B G, Kim K S, Kim K Y, Ahn J W, Kim T G, Kim K R, Jang Y H, Lee S U 2011 Test method of cavitation erosion for marine coatings with low hardness *Ocean Eng.* **38**(13) 1495-1502

[3] Ji B, Luo, X W, Arndt R E A, Peng X X, Wu Y L 2015 Large eddy simulation and theoretical investigation of the transient cavitating vortical flow structure around a NACA66 hydrofoil *Int. J. Multiph. Flow* **68** 121-134

[4] Amromin E, Kovinskaya S 2000.Vibration of cavitating elastic wing in a periodically perturbed flow: excitation of subharmonics *J. Fluids Struct.* **14**(5) 735-751
[5] Torre O, Escaler X, Egusquiza E, Farhat M 2013 Experimental investigation of added mass effects on a hydrofoil under cavitation conditions *J. Fluids Struct.* **39** 173-187
[6] Ausoni P, Farhat M, Escaler X, Egusquiza E, Avellan F 2007 Cavitation influence on von kármán vortex shedding and induced hydrofoil vibrations *ASME J. Fluids Eng.* **129** 966-973
[7] Young Y L, Chae E J, Akcabay D T 2012 Hybrid algorithm for modeling of fluid-structure interaction in incompressible viscous flows *Acta Mech. Sinica.* **28**(4) 1030-1041
[8] Wu Q, Huang B, Wang G Y, Gao Y 2015 Experimental and numerical investigation of hydroelastic response of a flexible hydrofoil in cavitating flow *Int. J. Multiph. Flow* **74** 19-33
[9] Strang G, Nguyen T 1996 Wavelets and filter banks Wellesley-Cambridge Press
[10] Menter F R 1992 Improved two-equation *k-ω* turbulence models for aerodynamic flows *NASA Technical Memorandu.* **34** 103975
[11] Coutier-Delgosha O, Fortes-Patella R, Reboud J L 2003 Evaluation of the turbulence model influence on the numerical simulations of unsteady cavitations *ASME J. Fluids Eng.* **125**(1) 38-45
[12] Huang B, Ducoin A, Young Y L 2012 Evaluation of cavitation models for prediction of transient cavitating flows around a pitching hydrofoil *Proceedings of the 8th International Symposium on Cavitations*, Research Publishing Services, Singapore
[13] Kubota A, Kato H, Yamaguchi H 1992 A new modeling of cavitating flows: a numerical study of unsteady cavitation on a hydrofoil section *J. Fluid Mech.* **240** 59-96
[14] Zwart P, Gerber A, Belamri T 2004 A two-phase flow model for predicting cavitation dynamics *The* 5th *International Conference* on *Multiphase Flow,* Yokohama, Japan
[15] Theodorsen T 1935 General theory of aerodynamic instability and the mechanism of flutter National Advisory Committee for Aeronautics, Technical Report, No. 496
[16] Huang B, Young Y L, Wang G Y, Shyy W 2013 Combined experimental and computational investigation of unsteady structure of sheet/cloud cavitation *J. Fluids Eng.* **135**(7) 071301